

The Galactic chemical evolution of phosphorus observed with IGRINS*

G. Nandakumar¹, N. Ryde¹, M. Montelius², B. Thorsbro³, H. Jönsson⁴, and G. Mace⁵

- ¹ Lund Observatory, Department of Astronomy and Theoretical Physics, Lund University, Box 43, 221 00 Lund, Sweden e-mail: govind.nandakumar@astro.lu.se
- ² Kapteyn Astronomical Institute, University of Groningen, Landleven 12, 9747 AD Groningen, The Netherlands
- ³ Department of Astronomy, School of Science, The University of Tokyo, 7-3-1 Hongo, Bunkyo-ku, Tokyo 113-0033, Japan
- ⁴ Materials Science and Applied Mathematics, Malmö University, 205 06 Malmö, Sweden
- Department of Astronomy and McDonald Observatory, The University of Texas, Austin, TX 78712, USA

Received 9 August 2022 / Accepted 10 October 2022

ABSTRACT

Context. Phosphorus (P) is considered to be one of the key elements for life, making it an important element to look for in the abundance analysis of spectra of stellar systems. Yet, only a select number of spectroscopic studies exist to estimate the phosphorus abundances and investigate its trend across a range of metallicities. This is due to the lack of good phosphorus lines in the optical wavelength region and the requirement of careful manual analysis of the blended phosphorus lines in near-infrared H-band spectra obtained with individual observations and surveys such as the Apache Point Observatory Galactic Evolution Experiment (APOGEE). Aims. Based on a consistent and systematic analysis of high-resolution, near-infrared Immersion GRating INfrared Spectrograph (IGRINS) spectra of 38 K giant stars in the Solar neighborhood, we present and investigate the phosphorus abundance trend in the metallicity range of -1.2 dex < [Fe/H] < 0.4 dex. Furthermore, we compare this trend with the available chemical evolution models to shed some light on the origin and evolution of phosphorus.

Methods. We have observed full H- and K-band spectra at a spectral resolving power of $R=45\,000$ with IGRINS mounted on the Gemini South telescope, the Discovery Channel Telescope, and the Harlan J Smith Telescope at McDonald Observatory. Abundances were determined from spectral lines by modeling the synthetic spectrum that best matches the observed spectrum by χ^2 minimization. For this task, we used the Spectroscopy Made Easy (SME) tool in combination with one-dimensional (1D) Model Atmospheres in a Radiative and Convective Scheme (MARCS) stellar atmosphere models. The investigated sample of stars have reliable stellar parameters estimated using optical Fiber-fed Echelle Spectrograph (FIES) spectra obtained in a previous study of a set of stars called Glants in the Local Disk (GILD). In order to determine the phosphorus abundances from the 16482.92 Å phosphorus line, we needed to take special care blending the $CO(\nu = 7-4)$ line. With the stellar parameters known, we thus determined the C, N, and O abundances from atomic carbon and a range of nonblended molecular lines (CO, CN, and OH) which are plentiful in the H-band region of K giant stars, assuring an appropriate modeling of the blending $CO(\nu = 7-4)$ line.

Results. We present the [P/Fe] versus [Fe/H] trend for K giant stars in the metallicity range of $-1.2 \, \text{dex} < [\text{Fe/H}] < 0.4 \, \text{dex}$ and enhanced phosphorus abundances for two metal-poor s-rich stars. We find that our trend matches well with the compiled literature sample of prominently dwarf stars and the limited number of giant stars. Our trend is found to be higher by $\sim 0.05-0.1 \, \text{dex}$ compared to the theoretical chemical evolution trend resulting from the core collapse supernova (type II) of massive stars with the phosphorus yields arbitrarily increased by a factor of 2.75. Thus the enhancement factor might need to be $\sim 0.05-0.1 \, \text{dex}$ higher to match our trend. We also find an empirically determined primary behavior for phosphorus. Furthermore, the phosphorus abundance is found to be elevated by $\sim 0.6-0.9 \, \text{dex}$ in the two s-enriched stars compared to the theoretical chemical evolution trend.

Key words. stars: abundances – stars: late-type – Galaxy: evolution – Galaxy: disk – infrared: stars

1. Introduction

Analogous to fossils here on Earth, light from stars can be used to understand the formation and evolution history of stellar populations. This is possible through detailed spectroscopic analysis of stellar spectra from which chemical compositions of each star and hence their parent molecular clouds can be determined. Individual elemental abundances derived from stellar spectra in conjunction with chemical evolution models have also been used to infer their nucleosynthetic origin, trace possible star progenitors, predict their stellar yields, and impose constraints

on their formation inside stars. For example, α elements such as O, Mg, Si, Ca, and Ti are formed in massive stars during hydrostatic and explosive burning phases, and they are released to the interstellar medium (ISM) when they undergo a type II supernova (SN) explosion (Chieffi & Limongi 2004; Nomoto et al. 2013; Matteucci 2021).

There are many elements whose origin and formation sites are still under debate or unknown. This is due to various reasons, such as an absence of measurable lines in commonly observed wavelength ranges, unreliable or unmeasured atomic data, and weak or strong lines that are difficult to model. Until a decade ago, phosphorus had been one such element that remained unexplored in long-lived stars of spectral type F, G, or K owing to the absence of phosphorus lines in the commonly observed wavelength ranges of these stars (Struve 1930; Caffau et al. 2011). Phosphorus is specifically interesting since it is among

^{*} Table of stars with stellar parameters and phosphorus abundances are only available at the CDS via anonymous ftp to cdsarc.cds.unistra.fr (130.79.128.5) or via https://cdsarc.cds.unistra.fr/viz-bin/cat/J/A+A/668/A88

the key elements for biology on Earth: H, C, N, O, P, and S. Assuming a 1:1 correlation between the elemental abundance in the star and the material out of which planets form, the detection of phosphorus in exoplanet hosts could prove useful in the search for life (Hinkel et al. 2020). Thus, it is important to identify and model measurable phosphorus lines for which a reliable phosphorus abundance can be determined for large stellar samples. It will then be possible to investigate the origin and evolution of phosphorus based on the comparison of its observed trend versus metallicity and other elements to those predicted by chemical evolution models.

One of the first attempts to investigate the phosphorus trend with metallicity was by Caffau et al. (2011) with phosphorus abundances measured from the infrared weak P I lines of the multiplet 1, at 1050-1082 nm in the CRyogenic highresolution InfraRed Echelle Spectrograph (CRIRES) spectra for 20 cool dwarf stars in the Galactic disk. They showed a decreasing trend of [P/Fe] with increasing metallicity in the range of -1.0 < [Fe/H] < 0.3 dex, which is different from the trend they found for other light odd-Z elements, sodium and aluminum. These abundance measurements were used by Cescutti et al. (2012) to construct and compare chemical evolution models with phosphorus and metallicity yields from Woosley & Weaver (1995) and Kobayashi et al. (2006) and they found that yields from massive stars have to be increased by a factor of 2.75 to match the observational trend. Jacobson et al. (2014) and Roederer et al. (2014) extended the lower metallicity range of the [P/Fe] versus [Fe/H] trend down to -3.8 dex determining an upper limit value for [P/Fe] with a P I doublet in the ultraviolet, 2135.465 Å and 2136.182 Å, using the *Hubble* Space Telescope-Space Telescope Imaging Spectrograph (STIS; Kimble et al. 1998; Woodgate et al. 1998). Using near-infrared (NIR) high resolution spectrograph GIANO (Origlia et al. 2014) at Telescopio Nazionale Galileo (TNG), and with the same lines used in Caffau et al. (2011, 2016, 2019), a consistent phosphorus trend with metallicity using ~43 stars was found. Similarly, Maas et al. (2017, 2019) estimated phosphorus abundances for FGK dwarfs, giants, and Hyades open cluster members using the aforementioned P I lines based on observations with the Phoenix high-resolution spectrometer (Hinkle et al. 1998) on the Kitt Peak National Observatory Mayall 4m telescope and the Gemini South telescope. They also found consistent [P/Fe] versus [Fe/H] trends with the literature and estimated solar values for abundance ratios of phosphorus with elements such as O, Mg, Si, and Ti pointing toward a similar formation site for phosphorus as these elements. Using spectra observed with the Habitable zone Planet Finder (HPF) on the 10 m Hobby–Eberly Telescope (HET) at McDonald Observatory (Mahadevan et al. 2012, 2014), Sneden et al. (2021) estimated phosphorus abundances from the same set of P I lines for 13 field red horizontal branch (RHB) stars. Very recently, Maas et al. (2022) used spectra from the same instrument to estimate phosphorus abundances for a sample of 163 FGK dwarfs and giants, and they found thick disk stars to have approximately 0.1 dex higher [P/Fe] than thin disk stars.

Among the large-scale spectroscopic surveys, the Apache Point Observatory Galactic Evolution Experiment/APOGEE (Majewski et al. 2017), which observe in the NIR H-band (15 100–17 000 Å, $R\sim22\,500$) regime, have identified two P I lines, 15711.1 and 16482.9 Å (Shetrone et al. 2015). However, the industrial pipeline used by APOGEE to analyze the spectra is not optimal for weak and blended lines such as these. Hence, APOGEE DR12 does not include phosphorus abundance

measurements (Holtzman et al. 2015). However, Hawkins et al. (2016) reanalyzed APOGEE spectra for the APOGEE+Kepler stellar sample (APOKASC) of ~2000 giants with the Brussels Automatic Code for Characterizing High accUracy Spectra (BACCHUS) code (Masseron et al. 2016) and estimated phosphorus abundances from the aforementioned two lines, finding a decreasing [P/Fe] trend with increasing metallicity. The recent data releases, APOGEE DR13–DR16 (e.g., Jönsson et al. 2018), include phosphorus though it is cautioned to be one of the most uncertain elements in APOGEE. As a result, for the latest data release of APOGEE (DR17, Holtzman et al., in prep.), it was decided not to include any phosphorus abundances. However, Hayes et al. (2022) carried out a reanalysis of APOGEE data with BACCHUS to measure phosphorus, among other difficult-to-measure elements in APOGEE.

A similar type of reanalysis of APOGEE spectra led to the discovery of 15 P-rich stars by Masseron et al. (2020a). The elemental abundance patterns of these stars with enhanced Mg, Si, Al, and s-process elements have challenged theoretical models, suggesting these over abundances could have formed from a new s-process site (Masseron et al. 2020b). The same two phosphorus lines in higher resolution ($R \sim 45\,000$) Immersion GRating INfrared Spectrograph (IGRINS) spectra have been used by Afşar et al. (2018b), and Böcek Topcu et al. (2019, 2020) to estimate [P/Fe] for three field RHB stars and approximately ten giant stars in the open clusters NGC 6940 and NGC 752, respectively.

The abovementioned studies indicate a dearth of reliable phosphorus abundance estimates, especially for giant stars. Even though giants are less interesting in the context of searching for habitable planets, they allow us to probe more distant populations. Thus there is an evident necessity for more high resolution spectroscopic observations as well as a systematic analysis to increase the sample size of stars with reliable phosphorus estimates, especially for giant stars. Here, we present a consistent, detailed, and systematic analysis of the phosphorus line at 16482.92 Å in the high resolution NIR *H*-band IGRINS spectra of 38 K giant stars in the solar neighborhood to determine their phosphorus abundances. Our sample of stars are a subset of the GIants in the Local Disk (GILD) sample (in the same way as Ryde et al. (2020) and Montelius et al. (2022)), and they have reliable stellar parameters determined from optical FIber-fed Echelle Spectrograph (FIES) spectra. In Sect. 2, we briefly describe the IGRINS observations and data reduction carried out to obtain the final spectra. An explanation of how phosphorus was determined from spectra using Spectroscopy Made Easy (SME) is described in Sect. 3, followed by the results and a discussion in Sects. 4 and 5, respectively. Finally, we make concluding remarks in Sect. 6.

2. Observations and data reduction

For this work, we carried out NIR spectroscopic observations of 38 K giant stars with IGRINS (Yuk et al. 2010; Wang et al. 2010; Gully-Santiago et al. 2012; Moon et al. 2012; Park et al. 2014; Jeong et al. 2014) in 2016 on the 4.3-m Discovery Channel Telescope (DCT; now called the Lowell Discovery Telescope) at Lowell Observatory (Mace et al. 2018), and on the 2.7-m Harlan J. Smith Telescope at McDonald Observatory (Mace et al. 2016), as well as on Gemini South telescope (Mace et al. 2018) in early 2022 as part of the poor-weather programs GS-2021B-Q416 and GS-2022A-Q408. IGRINS provides spectra spanning the full H and K bands (1.45–2.5 μ m) with a spectral resolving power of $R \sim 45\,000$. Details about the observations are listed in Table 1.

Table 1. Observational details of K giant stars.

Star	2MASS ID	$\begin{array}{c} H_{2MASS} \\ (mag) \end{array}$	$\begin{array}{c} K_{2MASS} \\ (mag) \end{array}$	Civil Date	Telescope	Exposure s
μleo	J09524585+2600248	1.3	1.2	2016 Jan. 31	HJST	26
εVir	J13021059+1057329	0.9	0.8	2016 Feb. 2	HJST	26
β Gem	J07451891+2801340	-1.0	-1.1	2016 Jan. 30	HJST	23
HD 102328	J11465561+5537416	2.9	2.6	2016 Feb. 2	HJST	32
HIP50583	J10195836+1950290	-0.8	-0.8	2016 June 20	HJST	29
HIP63432	J12595500+6635502	2.4	2.1	2016 May 29	HJST	180
HIP72012	J14434444+4027333	2.6	2.4	2016 June 16	HJST	120
HIP90344	J18255915+6533486	2.2	2.1	2016 June 15	HJST	120
HIP96014	J19311935+5018240	2.9	2.5	2016 June 15	HJST	120
HIP102488	J20461266+3358128	0.2	0.1	2016 June 19	HJST	26
2M16113361	J16113361+2436523	7.9	7.7	2016 July 26	HJST	180
2M17215666	J17215666+4301408	7.6	7.5	2016 July 25	HJST	1080
KIC3748585	J19272877+3848096	6.4	6.3	2016 Nov. 17	DCT	240
KIC3936921	J19023934+3905592	8.3	8.1	2016 Nov. 23	DCT	120
KIC3955590	J19272677+3900456	7.8	7.7	2016 Nov. 23	DCT	480
KIC4659706	J19324055+3946338	7.6	7.4	2016 Nov. 19	DCT	480
KIC5113061	J19413439+4017482	8.2	8.0	2016 Nov. 22	DCT	90
KIC5113910	J19421943+4016074	8.2	8.0	2016 Nov. 22	DCT	720
KIC5709564	J19321853+4058217	7.6	7.5	2016 Nov. 23	DCT	480
KIC5779724	J19123427+4105257	8.0	7.8	2016 Dec. 09	DCT	600
KIC5859492	J19021718+4107236	7.9	7.8	2016 Nov. 23	DCT	480
KIC5900096	J19515137+4106378	6.0	5.8	2016 Nov. 22	DCT	120
KIC6465075	J19512404+4149284	8.0	7.9	2016 Nov. 23	DCT	480
KIC6837256	J18464309+4223144	8.8	8.7	2016 Nov. 23	DCT	720
KIC7006979	J18433894+4235295	7.5	7.6	2016 Nov 18	DCT	90
KIC10186608	J18444919+4717434	8.9	8.8	2016 Nov. 17	DCT	960
KIC11045542	J19530590+4833180	8.4	8.2	2016 Dec. 11	DCT	2000
KIC11342694	J19110062+4906529	7.6	7.4	2016 Nov. 17	DCT	480
KIC11444313	J19014380+4923062	9.1	9.0	2016 Nov. 23	DCT	720
KIC11569659	J19464387+4934210	9.4	9.3	2016 Dec. 9	DCT	2400
ksiHya	J11330013-3151273	1.5	1.4	2016 June 30	HJST	8
HD 175541	J18554089+0415551	5.9	5.8	2022 May 09	Gemini South	80
HD 176981	J19022156+0822248	2.6	2.5	2022 May 24	Gemini South	8
HD 206610	J21432490-0724296	6.1	5.9	2022 May 24	Gemini South	80
HD 76445	J08564599+1728530	5.4	5.3	2022 Jan. 24	Gemini South	20
NGC 6705 1184	J18513901-0613070	10.6	10.4	2022 May 09	Gemini South	160
NGC 6705 1423	J18505581-0618147	7.9	7.7	2022 May 24	Gemini South	200

Notes. DCT: the Discovery Channel Telescope, a 4.3 m telescope at Lowell Observatory, Arizona. HJST: the Harlan J Smith Telescope, a 2.7 m telescope at McDonald Observatory, Texas. Gemini South: 8.1-m Gemini South telescope.

We selected the stars from among nearly 500 local disk giants from the observing program with FIES (Telting et al. 2014) at the Nordic Optical Telescope (NOT) started in Jönsson et al. (2017). The stellar parameters for these stars have been determined through a careful optical spectroscopic analysis using the same tools for the spectral analysis as presented here (Jönsson et al., in prep.). We also used the high resolution ($R \sim 100\,000$) infrared spectrum of Arcturus from the Arcturus atlas (Hinkle et al. 1995).

The IGRINS observations were carried out in an ABBA nod sequence along the slit, permitting sky background subtraction. With the aim of achieving signal-to-noise ratios (S/Ns) of at least 100, exposure times were set to ~10–2500 s. Telluric standard stars were chosen to be rapidly rotating, late B to early A dwarfs and observed close in time and at a similar air mass as the science targets. We used the IGRINS PipeLine Package (IGRINS PLP; Lee et al. 2017) to optimally extract the telluric-corrected,

wavelength-calibrated spectra after flat-field correction and A–B frame subtraction. The spectral orders of the science targets and the telluric standards were subsequently stitched together after normalizing every order and then combining them in iraf (Tody 1993), excluding the low S/N edges of every order. This resulted in one normalized stitched spectrum for the entire H band. However, to take care of any modulations in the continuum levels of the spectra, we paid a lot of attention to define specific local continua around the spectral line being studied. This turns out to be an important measure for accurate determinations of abundances; see for example, Santos-Peral et al. (2020).

The standard procedure for eliminating the contaminating telluric lines is to divide the star spectrum with a telluric standard-star spectrum, showing only telluric lines and mostly no stellar features. This works very well for most wavelength regions. Apart from some broad Brackett lines of hydrogen, some spurious broadband spectral features might, however, turn

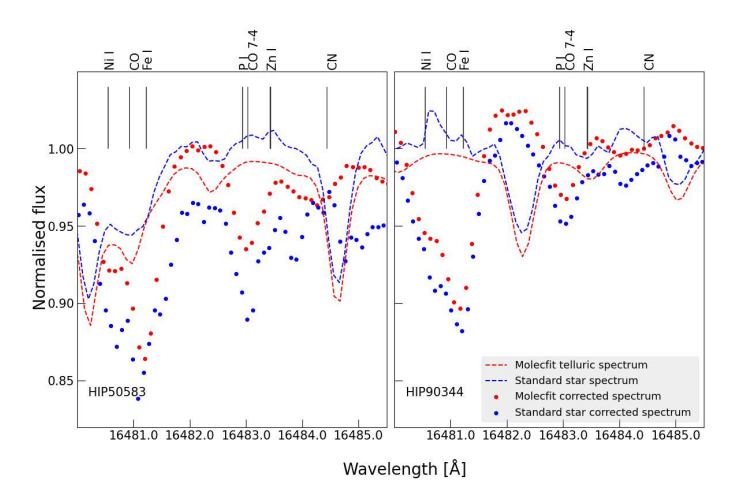


Fig. 1. Molecfit-corrected spectrum (red dots) and the standard star-corrected spectrum (blue dots) around the P I line at 16482.92 Å for two stars in our sample. The normalized telluric spectra from the standard star observation and from using the Molecfit software tool are shown with a blue-dashed line and red-dashed line, respectively. Since the telluric standard star spectra show unexpected spurious features at the wavelengths of the phosphorus line, we eliminated the telluric lines with Molecfit. Using the standard star spectra with the spurious emission feature would lead to an artificial increase in the strength of the P I line.

up in the telluric standard-star spectrum. For many of our observed stars, the corresponding telluric standard-star spectra indeed show broadband (ranging over more than 5 Å, i.e., over several resolution elements) and nonflat features affecting the normalized science spectra just in the wavelength region of the phosphorus line. No such features are expected in the telluric spectrum in this wavelength region, where only CH₄ absorption lines are expected. These observed spurious problems with the telluric standard-star spectra therefore make a proper continuum normalization of the science spectra impossible. In order to rectify this problem, we therefore carried out telluric correction using the Molecfit software tool (Smette et al. 2015; Kausch et al. 2015) for the spectra surrounding the phosphorus line. This tool models and fits the telluric lines in the observed science spectrum for various telluric molecules (H₂O, CO₂, CH₄, O₂, etc.). Molecfit requires the temperature, pressure, and humidity during the time of the target observation as inputs in order to model the Earth's atmosphere using a state-of-the-art radiative transfer code. The Molecfit GUI tool also provides the option to choose the wavelength regions to be included (strong telluric lines) and thus to define masks, which are then used to identify the lines that need to be fitted. Finally, the model parameters obtained by fitting the chosen lines (masks) are used to model the telluric spectrum in the full wavelength range with which the science spectrum is corrected. Figure 1 shows the difference between the Molecfit-corrected spectrum (red dots) and the standard star-corrected spectra (blue dots) for two stars in our sample. The telluric spectra from the standard star observations (blue-dashed lines) with problematic continuum normalization result in artificially stronger lines, especially for our line of interest at 16481.92 Å. Meanwhile, the telluric spectra from Molecfit (red-dashed lines) show a reliable continuum normalization and thus provide telluric-corrected science spectra from which the phosphorus abundance can be determined.

In all our spectral plots, we also show the corresponding telluric spectra from Molecfit (in yellow) which were used to eliminate the telluric lines. We did this in order to show how good the elimination procedure actually works. Furthermore, it also shows where the telluric lines originally lay and where the S/N, therefore, is expected to be lower, as well as where spectral residuals might sometimes be identified, especially from the strongest telluric features.

Finally, for the wavelength solutions, sky OH emission lines were used (Han et al. 2012; Oh et al. 2014) and the spectra were subsequently shifted to laboratory wavelengths in air after a stellar radial velocity correction. In addition, we made sure to carefully eliminate obvious cosmic-ray signatures in the spectra.

3. Analysis

3.1. Phosphorus lines in IGRINS

There are two phosphorus lines in the H-band spectra that have been used in the literature: the lines at 15711.52 Å and 16482.92 Å. Upon initial checks, the line at 15711.52 Å in our spectra is found to be severely affected by telluric lines, making a phosphorus abundance determination with this line impossible. Hence we only use the line at 16482.92 Å in our analysis. For this line, there is a theoretically determined log(qf) = -0.27(Biemont et al. 1994), but when using this value, the line is synthesized too strongly in the solar spectrum. For this reason, Afşar et al. (2018a) determined an astrophysical log(gf) value of -0.56for this line by applying reverse solar analysis using the high resolution infrared solar flux spectrum of Wallace & Livingston (2003) and a solar phosphorus abundance value of 5.41 from Asplund et al. (2009). Similarly we determined an astrophysical log(qf) value of -0.51 based on reverse solar analysis with the same solar flux spectrum. The difference of 0.05 with respect to the value from Afşar et al. (2018a) is due to the lower solar phosphorus abundance value of 5.36 we adopted from Grevesse et al. (2007). We also determined astrophysical log(gf) values based on reverse solar analysis for the spectral lines of light odd-Z (Na, Al, and K) and even-Z elements (Mg, Si, and S) used in this work (see Sect. 5.2 and Table A.1).

Due to the odd number of protons in the phosphorus nucleus, the spectral lines are likely to be affected by hyperfine structure splitting (see e.g., Pendlebury & Smith 1964). The line we measured our abundances from does not have information on the strength of the hyperfine structure splitting; however, as the line is weak, we do not expect it to impact our results significantly.

For the molecular lines, we used the line data for CO from Li et al. (2015), for CN from Sneden et al. (2014), and for OH from Brooke et al. (2016). In the section below, we explain the determination of the phosphorus abundance from this line in detail.

3.2. Determination of the phosphorus abundance

We determined the phosphorus abundance from the observed spectra using the SME Valenti & Piskunov (1996, 2012) code which generates synthetic spectra for a set of stellar parameters by calculating the radiative transfer and interpolating in a grid of hydrostatic one-dimensional (1D) Model Atmospheres in a Radiative and Convective Scheme (MARCS) stellar atmosphere models (Gustafsson et al. 2008) in spherical geometry, assuming local theormodynamic equilibrium (LTE), chemical equilibrium, homogeneity, and conservation of the total flux. SME generates and fits multiple synthetic spectra for the chosen line of interest by varying its elemental abundance (set as a free parameter). The final abundance of the line is chosen to be the one that corresponds to the synthetic spectrum that best matches the observed spectrum by means of the χ^2 minimization method.

Table 2. Stellar parameters, stellar population from Jönsson et al., (in prep.), as well as v_{macro} , [P/Fe], σ [P/Fe], and the signal-to-noise ratio (S/N) determined in this work.

Star	Population	$T_{ m eff}$ K	$\log g \\ \log(\mathrm{cm}\mathrm{s}^{-2})$	[Fe/H] dex	$v_{ m micro} \ { m km \ s^{-1}}$	$v_{ m macro} \ { m km \ s^{-1}}$	[P/Fe] dex	σ [P/Fe] dex	S/N per pixel
<u>α</u> Boo ^(*)	Thick	4308	1.7	-0.55	1.8	4.9	0.44	0.12	297
μ Leo	Thin	4494	2.5	0.27	1.5	6.7	0.29	0.08	169
ϵ Vir	Thin	5112	3.0	0.11	1.6	7.7	-0.04	0.06	300
betaGem	thin	4809	2.8	-0.02	1.4	6.9	0.06	0.07	336
HD 102328	Thin	4442	2.5	0.28	1.5	7.1	0.12	0.08	250
HIP50583	Thin	4292	1.6	-0.54	1.6	5.6	0.44	0.06	86
HIP63432	Thick	4155	1.3	-0.87	1.9	7.5	0.4	0.07	275
HIP72012	Thin	4077	1.4	-0.28	1.5	6.3	0.28	0.08	285
HIP90344	Thin	4454	2.2	-0.39	1.4	7.0	0.1	0.06	282
HIP96014	Thin	4240	1.6	-0.43	1.7	7.8	0.36	0.08	414
HIP102488	Thin	4742	2.5	-0.21	1.6	6.0	0.16	0.1	343
2M16113361	halo,s-rich	4042	1.2	-1.06	1.9	6.4	0.93	0.09	160
2M17215666	halo,s-rich	4342	1.6	-1.11	1.6	6.7	1.2	0.06	165
KIC3748585	Thin	4569	2.6	0.03	1.3	5.6	-0.09	0.07	205
KIC3936921	Thick	4488	2.2	0.01	1.6	5.4	-0.04	0.05	130
KIC3955590	Thin	4411	2.2	0.03	1.6	5.7	0.09	0.1	140
KIC4659706	Thick	4428	2.5	0.24	1.4	5.4	0.09	0.06	86
KIC5113061	Thin	4100	1.6	-0.09	1.8	5.5	0.16	0.06	164
KIC5113910	Thin	4338	1.7	-0.48	1.6	6.2	0.37	0.08	182
KIC5709564	Thick	4687	2.2	-0.35	1.7	7.0	0.22	0.07	137
KIC5779724	Thick	4303	1.6	-0.45	1.6	5.7	0.54	0.09	215
KIC5859492	Thin	4511	2.4	0.09	1.5	5.5	0.24	0.06	180
KIC5900096	Thin	4480	2.5	0.23	1.5	5.6	-0.1	0.08	179
KIC6465075	Thin	4825	2.8	-0.37	1.3	5.5	0.13	0.09	146
KIC6837256	Thick	4731	2.3	-0.73	1.5	5.6	0.39	0.06	148
KIC7006979	Thin	4869	2.6	-0.34	1.6	5.3	0.46	0.06	104
KIC10186608	Thin	4676	2.5	-0.12	1.5	5.8	0.14	0.06	91
KIC11045542	Thin	4304	1.6	-0.65	1.5	5.9	0.17	0.06	294
KIC11342694	Thin	4509	2.8	0.14	1.3	5.3	-0.07	0.07	139
KIC11444313	Thin	4630	2.3	-0.18	1.5	5.3	0.29	0.09	160
KIC11569659	Thin	4838	2.4	-0.43	1.6	5.8	0.16	0.03	246
<i>ξ</i> Hya	Thin	5045	2.8	0.31	0.5	8.1	-0.1	0.06	176
HD 175541	Thin	5067	3.5	-0.15	1.2	3.7	-0.07	0.02	115
HD 176981	Thin	4095	1.6	-0.22	1.8	5.7	0.24	0.09	95
HD 206610	Thick	4849	3.3	0.04	1.2	3.2	0.08	0.1	152
HD 76445	Thick	4836	3.1	-0.22	1.4	3.6	0.17	0.08	111
NGC 67051184	Thin	4282	1.6	-0.05	1.7	6.2	0.15	0.07	32
NGC 67051423	Thin	4377	1.8	0.03	1.9	7.4	0.19	0.09	38

Notes. (*)Infrared atlas spectrum of Arcturus (Hinkle et al. 1995).

As mentioned in Sect. 2, the stars analyzed in this work are a subset of the GILD stellar catalog (Jönsson et al., in prep., which builds upon and improves the analysis described in Jönsson et al. 2017). These stars were also used in, for example, Jönsson et al. (2017), Forsberg et al. (2019, 2022), Ryde et al. (2020), and Montelius et al. (2022). The fundamental stellar parameters, namely the effective temperature $(T_{\rm eff})$, surface gravity ($\log g$), metallicity ([Fe/H]), and microturbulence (ξ_{micro}) , are estimated from fitting synthetic spectra for unsaturated and unblended Fe I and Fe II lines, Ca I lines, and log g sensitive Ca I line wings, while T_{eff} , $\log g$, [Fe/H], ξ_{micro} , and [Ca/Fe] are set as free parameters in SME. They have been benchmarked against independently determined effective temperatures, $T_{\rm eff}$, from angular diameter measurements and surface gravities, $\log q$, from asteroseismological measurements (see Jönsson et al. 2017, for more details). With uncertainties of $\pm 50 \,\mathrm{K}$ for T_{eff} , $\pm 0.15 \,\mathrm{dex}$ for $\log g$, $\pm 0.05 \,\mathrm{dex}$ for [Fe/H], and $\pm 0.1 \,\mathrm{km}\,\mathrm{s}^{-1}$ for ξ_{micro} , we have precise stellar parameters.

The phosphorus abundance we determined from the line at 16482.92 Å is blended with a $CO(\nu = 7-4)$ line. Hence it is necessary to model the CO line as well as being possible to determine an accurate phosphorus abundance. Fortunately, vibrational-rotational lines from the $CO(\nu = 7-4)$ band occur close to each other at a regular spacing lying at wavelengths less than 10 Å apart. We can therefore verify that the blending CO line has been reliably modeled by inspecting the neighboring CO(v = 7-4) lines, which we have done in the same manner as in Montelius et al. (2022). We determined C, N, and O abundances using the 25 OH ($\nu = 2-0, 3-1, 4-2, 5-3$), 20 CN ($\nu = 0-1$, 1–2), ten CO lines, as well as two CO band heads ($\nu = 6$ –3, 8-5) in our IGRINS H-band spectra using SME. We find the neighboring CO(v = 7-4) lines to fit well, which ensures that the CO(v = 7-4) blend in the phosphorus feature can be properly taken into account. Table 2 lists the fundamental stellar parameters from optical spectra along with the C, N, O, and P abundances estimated from our IGRINS spectra for the stars in

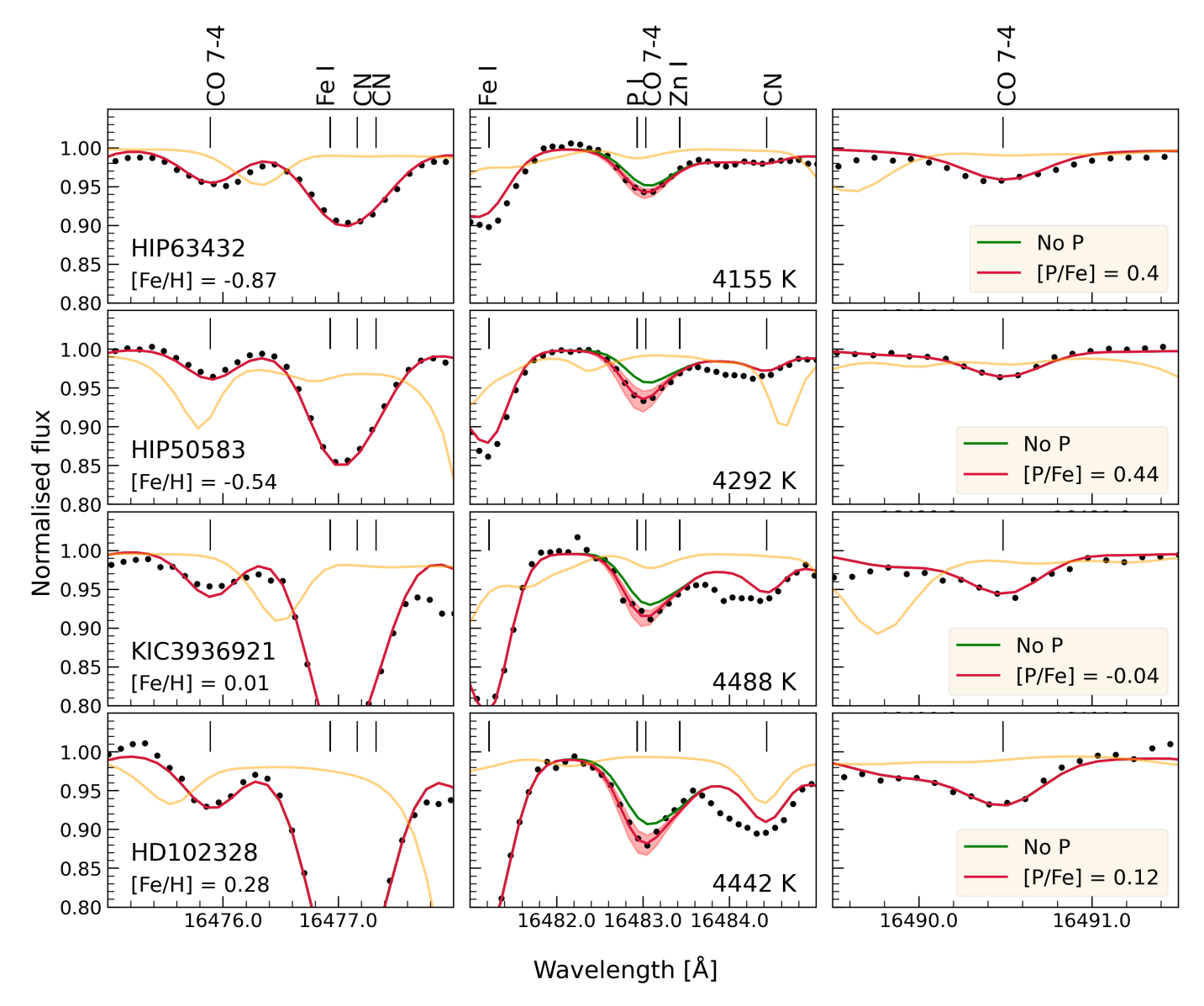


Fig. 2. Fits (red line) to the observed spectra (black points) for four stars chosen to represent the typical spectrum at metallicities of -0.87 dex (HIP63432), -0.54 dex (HIP50583), 0.01 dex (KIC3936921), and 0.28 dex (HD 102328). Each row represents one star with stars arranged in the order of increasing metallicity *from top to bottom*. The segment of the corresponding spectrum with the P line at 16482.92 Å is shown in the *middle panel in each row*. In the *left and right panels*, spectra of the neighboring CO(v = 7-4) lines are plotted. In each panel, the green line shows the synthetic spectrum without phosphorus or only showing the CO(v = 7-4) blend. The telluric spectrum used in the reduction is shown in yellow in order to indicate the pixels affected by telluric correction. The red band in the *middle panel* for the phosphorus line shows the variation of the synthetic spectrum with a $\Delta[P/Fe] = \pm 0.3$ dex variation. The effective temperature, T_{eff} , of each star is listed in the *middle panels*.

our sample. We adopted the solar abundance values for phosphorus ($A(P)_{\odot} = 5.36$), (and other elements in this study) from Grevesse et al. (2007) in the determination of the [P/Fe] values.

In Fig. 2, we show the fits (red line) to the observed spectra (black points) for four stars chosen to represent typical spectra at metallicities of -0.87 dex (HIP63432), -0.45 dex (HIP50583), 0.01 dex (KIC3936921), and 0.28 dex (HD 102328). Each row in Fig. 2 represents one star with the lowest metallicity star in the top row and the highest metallicity star in the bottom row. We show the segment of the corresponding spectrum with the phosphorus line at 16482.92 Å in the middle panel for each star (row). Synthetic and observed spectra of the neighboring $CO(\nu = 7-4)$ lines are plotted in the left and right panels to indicate the quality of the fit to the $CO(\nu = 7-4)$ line species, which in turn showcase the reliability of the phosphorus abundance

we estimated from the $CO(\nu = 7-4)$ blended phosphorus line. In addition, we show the sensitivity of the line to the phosphorus abundance value with the red band that shows the variation of the synthetic spectrum with a $\Delta[P/Fe] = \pm 0.3$ dex variation. This in turn gives a qualitative idea of the uncertainty as to the P I feature from the synthetic spectra fit. In each panel, we plotted the synthetic spectrum with no P I feature in green, that is to say showing only the $CO(\nu = 7-4)$ line which shows the contribution of phosphorus and CO features to the line. We also plotted the telluric spectra (in orange) used for telluric correction to highlight the noise introduced during telluric correction and how our line of interest is seldom affected by the noise. Thus, Fig. 2 shows the quality of our synthetic spectra fits and the reliability of the phosphorus abundance estimates listed in Table 2.

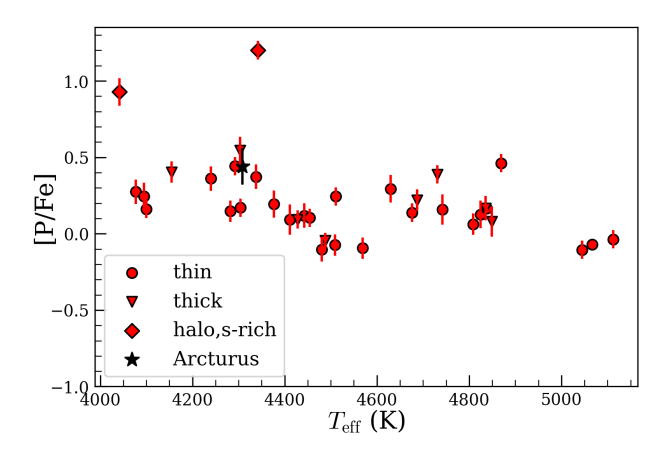


Fig. 3. [P/Fe] vs. $[T_{\rm eff}]$ for stars in our sample. Different symbols represent stellar populations to which each star belongs.

To investigate possible systematic effects such as any potential non-LTE effects, we plotted [P/Fe] as a function of $T_{\rm eff}$ in Fig. 3. We have used different symbols to indicate the stellar population of each star, that is, thin-disk, thick-disk, or halo, assigned based on their separation in the [Mg/Fe] versus [Fe/H] plane (see Jönsson et al. 2017; Lomaeva et al. 2019; Forsberg et al. 2019, for more details). Excluding the two halos that are s-rich and the three $T_{\rm eff} > 5000\,\rm K$ stars, there is no significant [P/Fe] trend with $T_{\rm eff}$. While s-rich stars have enhanced phosphorus abundances, the three 5000 K stars are metal rich and hence are expected to have lower phosphorus abundances. From the absence of any significant trend, we also conclude that the assumption that there are no significant non-LTE effects might be justified.

3.3. Uncertainty estimates

We determined the uncertainties in our [P/Fe] estimates that arise from the uncertainties in stellar parameters. As mentioned in the previous section, typical uncertainties in stellar parameters for our stars are estimated to be $\pm 50 \,\mathrm{K}$ for T_{eff} , $\pm 0.15 \,\mathrm{dex}$ for log g, ± 0.05 dex for [Fe/H], and ± 0.1 km s⁻¹ for ξ_{micro} . Using the stellar parameter value as the mean and these typical uncertainties as the standard deviation, we randomly generated sets of stellar parameters following a normal distribution and we reanalyzed each star spectrum using those parameters. We generated 50 sets of parameters for each star. Since the $CO(\nu = 7-4)$ lines are blended in the phosphorus feature, we redetermined the C, N, and O abundances for each set of stellar parameters in order for the blending line to fit. The resulting distribution of estimated [P/Fe] values was fitted with a Gaussian function. The dispersion estimated from the resulting fit gives the uncertainty in [P/Fe], listed in Table 2. In the same manner, we also determined the uncertainties in C, N, and O abundances, listed in Table A.2

We note that the sufficiently high S/N for our stars ensured that the observational noise played a minimal role in the uncertainty while fitting the synthetic spectra. In addition, we did not find a strong correlation between S/N and [P/Fe] uncertainty for stars with similar parameters, so other factors, such as a carbon abundance, could play a more important role in the uncertainty.

4. Results

4.1. [P/Fe] versus [Fe/H]

The metallicity of a star, [Fe/H], is considered to be an ideal parameter to compare and investigate the Galactic chemical

evolution of phosphorus of various stellar populations. In this section, we investigate the evolution of [P/Fe] as a function of [Fe/H] and we compare the resulting trend with those from the literature as well as theoretical chemical evolution models.

In Fig. 4, we plotted the [P/Fe] versus [Fe/H] trend for our K giants (in red) in the metallicity range of $-1.1 \le$ [Fe/H] \le 0.3 dex. There is a clear downward trend in [P/Fe] with increasing [Fe/H] which is slightly higher than the track of the chemical evolution model for phosphorus from Cescutti et al. (2012). They adopted the two-infall model of galactic chemical evolution and the phosphorus massive stellar yields from Kobayashi et al. (2006) which have been arbitrarily enhanced by a factor of 2.75 to match the observed trend in Caffau et al. (2011). Also this trend is similar to the trends seen for α elements (Si, Mg, O, etc.) that are primarily produced through core collapse SNe of massive stars with short lifetimes (order of millions of years).

We estimated a [P/Fe] of 0.44 ± 0.12 dex for Arcturus from the high resolution infrared atlas spectrum of Arcturus (Hinkle et al. 1995). We note that from the same atlas, but using the Y-band line of P I at 10581.5 Å, Maas et al. (2017) estimated a [P/Fe] of 0.27 ± 0.1 dex (rescaled to the solar phosphorus and Fe used in our study). Furthermore, Fanelli et al. (2021) estimated a [P/Fe] of 0.29 ± 0.06 dex (also rescaled) with a GIANO-B spectrum of Arcturus using P I lines at 10529.52 Å and 10581.58 Å. Our value is slightly higher than these noes; although, the values overlap within the uncertainties.

The [P/Fe] versus [Fe/H] trends for various samples from the literature rescaled based on the solar abundances of phosphorus and Fe used in this work are also plotted in Fig. 4. We could find only a select number of studies that analyze only giants: Afşar et al. (2018b), Böcek Topcu et al. (2019, 2020), and Sneden et al. (2021). The trends of which are shown in different colors (black) compared to other works. Afşar et al. (2018b) analyzed the IGRINS H- and K-band spectra of three field RHB stars with subsolar metallicity and used two phosphorus lines, 15711.5 A and 16482.9 Å, to estimate phosphorus abundance. Böcek Topcu et al. (2019, 2020) carried out a similar analysis of K giant stars in the open clusters NGC 6940 and NGC 752, respectively, using IGRINS spectra. Sneden et al. (2021) analyzed high resolution Habitable zone Planet Finder (HPF) spectra of 13 field RHB stars and one open cluster giant to estimate phosphorus abundances using three lines in the $0.81\text{--}1.28\,\mu\text{m}$ wavelength range. Metallicities for these stars are solar and lower, and the [P/Fe] estimates are consistent with our values.

While the APOGEE wavelength coverage includes the phosphorus lines used in this work and in Afşar et al. (2018b), the measurements of which are provided in data releases DR13–DR16, due to the reasons elaborated upon in Sect. 1. We do not include phosphorus abundances derived from the APOGEE spectra in the comparison sample.

Very recently, Maas et al. (2022) determined the phosphorus abundances for 163 stars from the P I line at 10529.52 Å based on observations with the HPF instrument on the Hobby–Eberly Telescope (HET). They find consistent abundances for both red giants and FGK dwarf stars, and an ~0.1 dex difference in [P/Fe] between thin and thick disk stars that were identified with kinematics. They also find [P/Fe] to be under-predicted by the Cescutti et al. (2012) model at lower metallicities ([Fe/H] < -0.5 dex), that is, they find a higher [P/Fe] for these stars. In Fig. 6, we plotted the running mean of the [P/Fe] as a function of [Fe/H] trends for the 163 stars from Maas et al. (2022; red line) and our measurements (blue line), excluding the two s-rich stars (see Sect. 4.2 below). The standard deviation within the

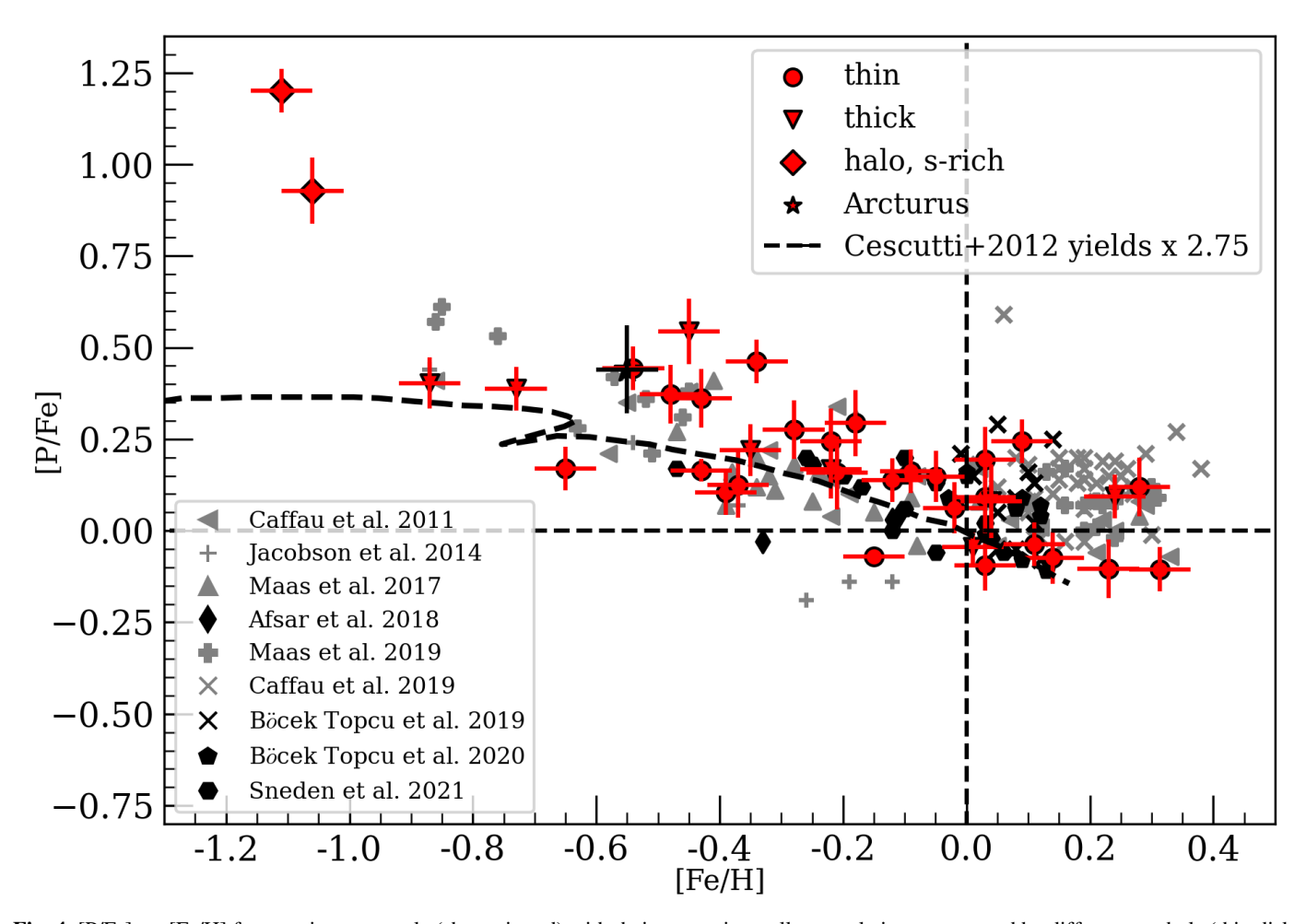


Fig. 4. [P/Fe] vs. [Fe/H] for stars in our sample (shown in red) with their respective stellar population represented by different symbols (thin disk, circle, thick disk, inverted triangle; and halo, s-rich, diamond). Arcturus, for which phosphorus was determined from the higher resolution atlas spectrum (Hinkle et al. 1995), is indicated by the black star symbol. Phosphorus abundance determinations (all scaled to the solar abundance used in this work: $A(P)_{\odot} = 5.36$ and $A(Fe)_{\odot} = 7.45$) from multiple literature sources are also plotted in gray (giants in black) and represented by different symbols. With a dashed line, we show the chemical evolution trend in Cescutti et al. (2012) resulting from the core collapse SN (type II) of massive stars with the phosphorus yields from Kobayashi et al. (2006) arbitrarily increased by a factor of 2.75.

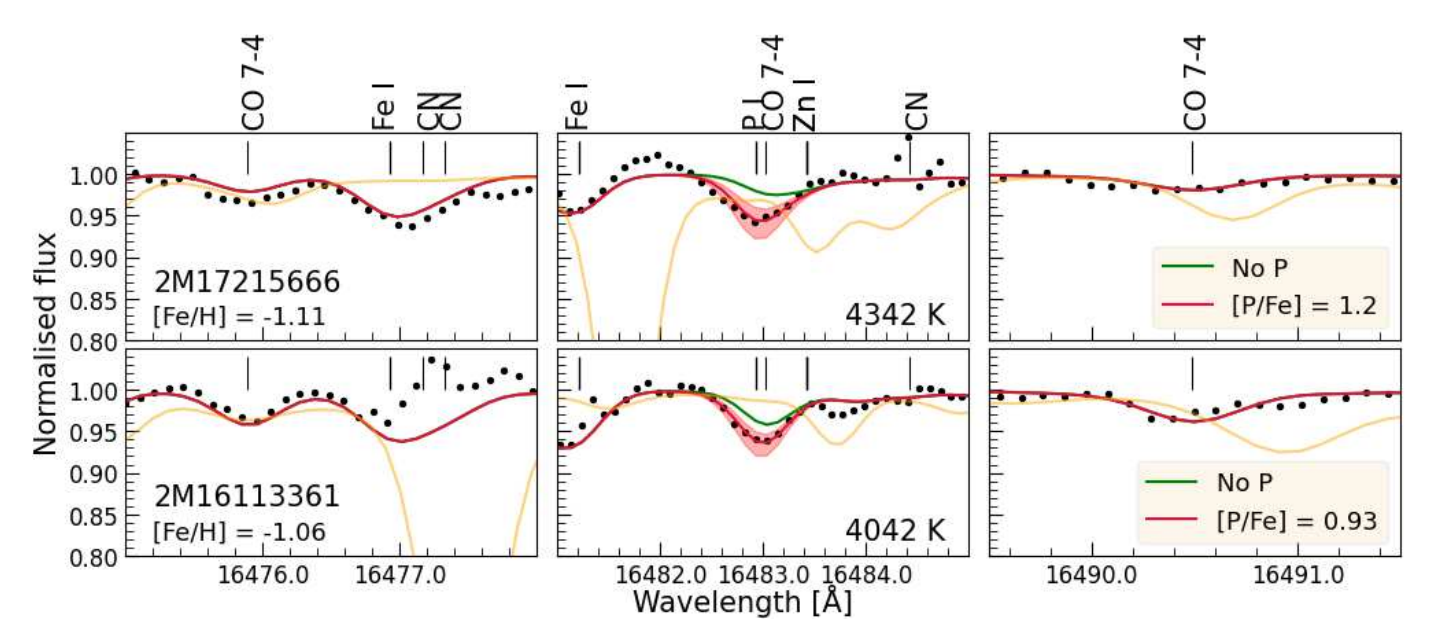


Fig. 5. Same as Fig. 2, except for the two s-rich stars in our sample.

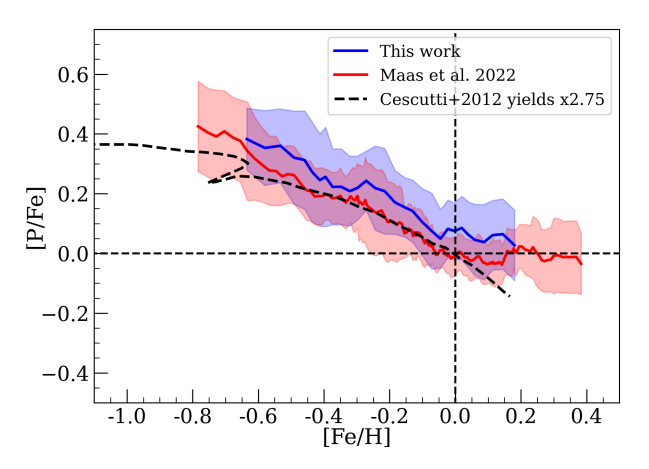


Fig. 6. Running mean of [P/Fe] for the stars in our sample (blue line) and the Maas et al. (2022) sample (red line) as a function of [Fe/H]. The standard deviation is represented by the blue and red bands for our sample and the Maas et al. (2022) sample, respectively. With a dashed line, we show the chemical evolution trend in Cescutti et al. (2012).

eight star bins for our sample and 15 star bins for the Maas et al. (2022) sample are represented by the blue and red bands, respectively. As mentioned above, the Maas et al. (2022) trend closely follows the Cescutti et al. (2012) model, except at lower metallicities and also at supersolar metallicities. Our trend is consistently higher by $\sim 0.05-0.1$ dex compared to both Maas et al. (2022) and the chemical evolution model trend. Both observational trends level off at supersolar metallicities as opposed to the chemical evolution trend that decreases to subsolar [P/Fe] values at these metallicities.

Comparing all of the samples from the literature, our trend is in unison with the trends from previous studies in the whole metallicity range within our estimated uncertainties. The [P/Fe] trend is found to level off for [Fe/H] > 0 in the comparison samples, which is also seen for the limited number of metal-rich stars in our sample. In chemical evolution models, for [P/Fe] to be constant and high at [Fe/H] > 0, an additional production or adjustments to the metallicity dependence of SNe yields may be needed. Thus, we need to analyze more metal-rich stars to confirm and understand possible mechanisms that lead to this trend.

4.2. s-rich stars

We find a distinct enhancement of \sim 0.6–0.9 dex for the two s-rich stars in our sample when compared with the Cescutti et al. (2012) model of phosphorus fitted to the Caffau et al. (2011) phosphorus trend of solar neighborhood stars. They have been identified to be rich in s-process elements (e.g., Ba and Ce) while normal in r-process and lighter elements from the analysis of their optical spectra (Forsberg et al. 2019). In Fig. 5, we show the fits (red line) to the observed spectra (black points) for these two stars. Similar to Fig. 2, fits to the neighboring $CO(\nu = 7-4)$ lines are shown in the left and right panels, and the red bands indicate the sensitivity of the phosphorus line to [P/Fe]. The fits along with the sensitivity band is a clear indicator that the enhancement in the phosphorus abundance for these stars is real, and not due to noise or telluric residuals.

Masseron et al. (2020a) identified 15 P-rich stars from APOGEE after reanalyzing their spectra using the BACCHUS code, finding [P/Fe] in the range of 1.2–2.2 dex. They also find enhanced O, Mg, Si, Al, and Ce as compared to the P-normal

stars. Based on a further detailed analysis of the high-resolution optical spectra of two previously confirmed phosphorus-rich stars in Masseron et al. (2020a,b) were able to find heavy-element over abundances with high first-peak (Sr, Y, and Zr) and second-peak (Ba, La, Ce, and Nd) element enhancements. While our P-rich stars are enhanced in Ce, we do not find enhancement in any other elements they report. In addition, [P/Fe] for these two P-rich stars are 0.93 and 1.2 dex, just below the minimum value of the [P/Fe] (1.2 dex) in the P-rich sample of Masseron et al. (2020a). Hence, these P-rich stars might be of a different class and origin and we believe that this warrants further detailed analyses of these stars.

5. Discussion

5.1. Nucleosynthesis of phosphorus

From chemical evolution models and multidimensional (2D and 3D) hydro-dynamical simulations of SN explosions (type I and II), the following formation channels for phosphorus have been suggested:

Firstly, the stable isotope of phosphorus, 31 P, is considered to be mainly synthesized from neutron capture on neutron-rich Si isotopes, 29 Si and 30 Si, which are all produced in the hydrostatic carbon and neon burning during the late stages of the evolution of massive stars (10–300 M_{\odot}), (Clayton 2003; Arnett 1996; Masseron et al. 2020a). It is then released by the explosion of these massive stars as type II SNe with insignificant phosphorus production predicted during the explosive phases by Woosley & Weaver (1995). Clayton (2003) concluded that 95% of phosphorus is formed in core-collapse type II SNe.

Secondly, ^{31}P is produced, though in negligible amounts, in low mass $(1\text{--}3~M_{\odot})$ asymptotic giant branch (AGB) stars by neutron capture on ^{30}Si (Karakas 2010). This is predicted to be accompanied by large enhancements of C and s-process elements by the stellar nucleosynthesis models.

In addition, Caffau et al. (2011) suggest phosphorus formation through proton captures on 30 Si and α captures on 27 Al. Also, Weinberg et al. (2019) find a possible SNIa contribution for phosphorus in the APOGEE DR14 data, which is contrary to what chemical evolution models find (Cescutti et al. 2012) with SNIa yields from Iwamoto et al. (1999). However, Weinberg et al. (2019) do warn about large statistical errors for phosphorus measurements in DR14, and, as already mentioned, phosphorus is not included in the final DR17 data release of APOGEE (Holtzman et al., in prep.).

For the neutron-capture production channel for light odd-Z elements, such as phosphorus, the production is sensitive to the neutron excess (Burbidge et al. 1957), which tends to decrease with decreasing metallicity (Kobayashi et al. 2006; Caffau et al. 2011) for metallicities lower than approximately [Fe/H] < -1. Our sample of stars do, unfortunately, not cover this metallicity range.

In the sections below, we attempt to decipher the nucleosynthetic origin of phosphorus based on the phosphorus abundance estimates from our sample. For this, we compare phosphorus with odd- and even-Z elements as well as investigate the primary and secondary behavior of phosphorus by comparing A(P) with A(Mg).

5.2. Comparison with odd- and even-Z elements

For the comparison, we chose the odd-Z elements Na, Al, and K and the even-Z elements Mg, Si, and S, and we determined their abundances from the IGRINS spectra with the lines listed

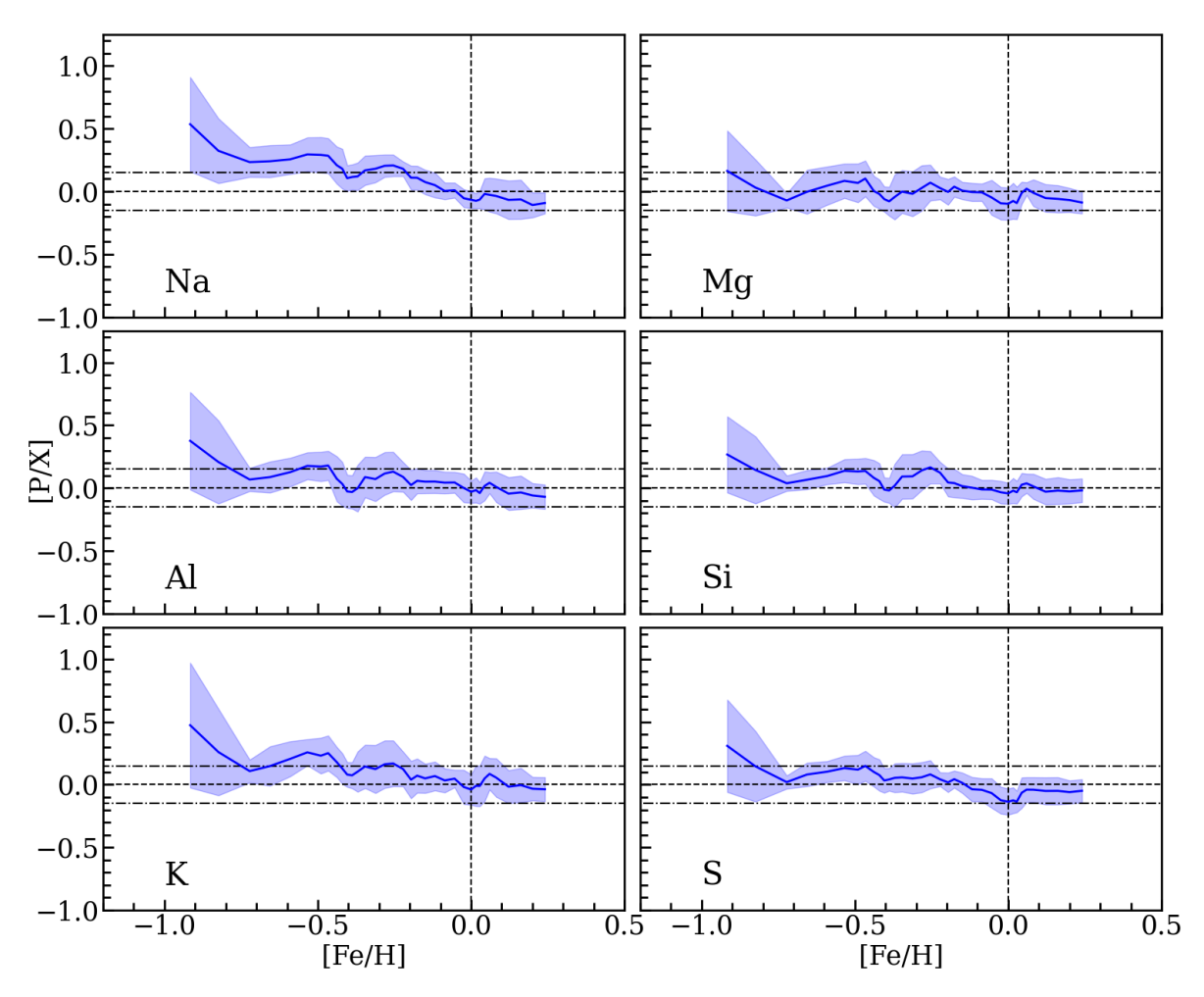


Fig. 7. Running mean of the abundance ratios of phosphorus to odd-Z (Na, Al, and K in the *left panels*) and even-Z (Mg, Si, and S in the *right panels*) as a function of [Fe/H]. The running mean and standard deviation are shown with the blue line and blue band, respectively. The mean value, $\langle [P/X] \rangle$ (excluding the two s-rich stars), is denoted in the bottom right part of each panel. Horizontal dash-dotted lines represent [P/X] values of ± 0.15 dex.

in Table A.1. We carried out a line-by-line analysis using SME (see Sect. 3.2) and chose the mean abundance for each species by a careful visual selection of the best fitting lines. The mean abundance was thus determined and the standard deviation of abundances from all of the chosen lines are listed in Table A.3. We plotted the running mean of the abundance ratios of phosphorus and these elemental abundances, [P/X], as a function of [Fe/H] in Fig. 7, with odd-Z elements and even-Z elements in the left and right panels, respectively. In each panel, the running mean and standard deviation are shown with the blue line and blue band, respectively.

We expect [P/X] ratios to be close to zero and not show any significant trends as a function of [Fe/H] if the evolution of phosphorus is similar to the element X with which it is compared. For all elements, the most metal-poor bin exhibits higher difference values since the two s-enhanced stars with high phosphorus values are included in this bin. In the case of Mg, Al, Si, and S, we find $[P/X] \sim 0$ with the running mean values lying within $[P/X] = \pm 0.15$ (horizontal dash-dot lines). The trend for [P/K] is close to 0 for [Fe/H] > -0.25 dex and increases for [Fe/H] < -0.25 dex. Thus [K/Fe] is not as enhanced as phosphorus in the metal-poor regime. For the remaining odd-Z element, Na, the [P/X] ratio has a decreasing trend with increasing metallicity. This is because [Na/Fe] has a near constant value of zero at subsolar metallicities which starts increasing

for supersolar metallicities and hence shows a different trend compared to P.

Magnesium, silicon, and sulphur are α elements that are confirmed to have been produced from core collapse SNe of massive stars (Chieffi & Limongi 2004; Nomoto et al. 2013). Similarly, Al and K are also found to have a significant contribution from core collapse SNe (for e.g., Clayton 2003; Weinberg et al. 2019, 2022). Thus we can conclude that phosphorus behaves similar to the α elements and this supports the current idea about the contribution of core collapse SNe in the origin and evolution of phosphorus. Similar investigations in previous studies have led to the same conclusion about the origin and evolution of phosphorus (see Sect. 1).

5.3. Primary behavior of Phosphorous for -0.9<[Fe/H]<0.3

Elements which are synthesized independently of the metallicity, that is elements produced in a star from chains of reactions starting directly from H and He, are called primary elements (Arnett 1996). The main isotopes of oxygen and magnesium, ¹⁶O and ²⁴Mg, are examples of primary elements (Clayton 2003). On the other hand, if the synthesis depends on the presence of other nuclei from earlier stellar generations, the elements produced are called secondary.

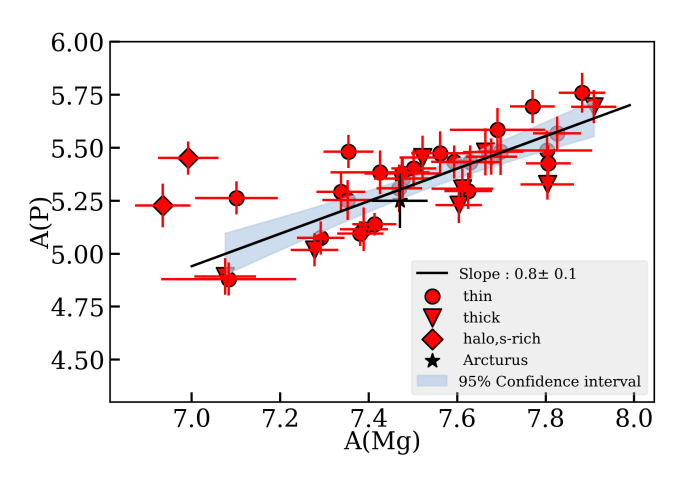


Fig. 8. Abundance of phosphorus, A(P), vs. the abundance of magnesium, A(Mg), for stars in our sample. Excluding the two s-rich stars from the sample, we estimate a slope of 0.8 ± 0.1 using linear regression, with the 95% confidence interval marked in blue. This points to a primary behavior of phosphorus similar to magnesium. We adopted solar abundance values of 5.36 and 7.53 for phosphorus and magnesium, respectively, from Grevesse et al. (2007).

The synthesis of phosphorus occurs due to neutron capture on neutron-rich Si isotopes, which are secondary in nature (Clayton 2003). One might therefore expect phosphorus to show a secondary behavior. In Fig. 8, we therefore plotted the phosphorus abundances versus the magnesium abundances. Since ²⁴Mg, a primary nuclei, is the main isotope of Mg (approximately 80% Clayton 2003), we assume that our measured Mg abundance represents a primary behavior. A secondary behavior for phosphorus would therefore yield a slope of 2. In Fig. 8 we, however, find a slope of 0.8 ± 0.1 for our sample using linear regression, excluding the s-element and P-rich stars, which clearly points to a primary behavior. We thus conclude that we find an empirically determined primary behavior of phosphorus, at least for the -0.9 < [Fe/H] < 0.3 range. This should be considered when the nucleosynthetic origin of phosphorus is investigated further. We note that Prantzos et al. (2018) indeed find a primary behavior in their rapidly rotating massive stars models.

5.4. Best stars to measure the P I line at 16482.92 Å

In this work, we have shown that it is possible to estimate reliable phosphorus abundances from the P I line at $16482.92 \,\text{Å}$ even though it can be heavily blended with a $\text{CO}(\nu = 7\text{--}4)$ line. In addition to careful manual analysis, that is to say selecting good continuum points, checking the fit to each spectrum by eye, and carefully inspecting the telluric elimination procedure, we made sure to fit the neighboring $\text{CO}(\nu = 7\text{--}4)$ lines well so as to determine the best phosphorus value.

Considering the dearth of phosphorus abundance measurements in the literature, we want to investigate which type of stars should be targeted in the future to get reliable phosphorus abundance estimates from this P I line. With that aim, we estimate the equivalent widths of the P I line and $CO(\nu = 7-4)$ line for a set of MARCS (Gustafsson et al. 2008) stellar models in a grid of (i) $3900 \le T_{\rm eff} \le 5000$ K, (ii) $1.0 \le \log g \le 3.0$, and (iii) [Fe/H] of -1.0, -0.5, 0.0, and 0.5 dex, all with solar-scaled phosphorus abundances. The resulting fractional contribution of equivalent widths of the P I line in the $CO(\nu = 7-4)$ blended line as a function of $T_{\rm eff}$ is shown in Fig. 9 with different combinations of [Fe/H] and a change in $\log g$ is represented by different colored

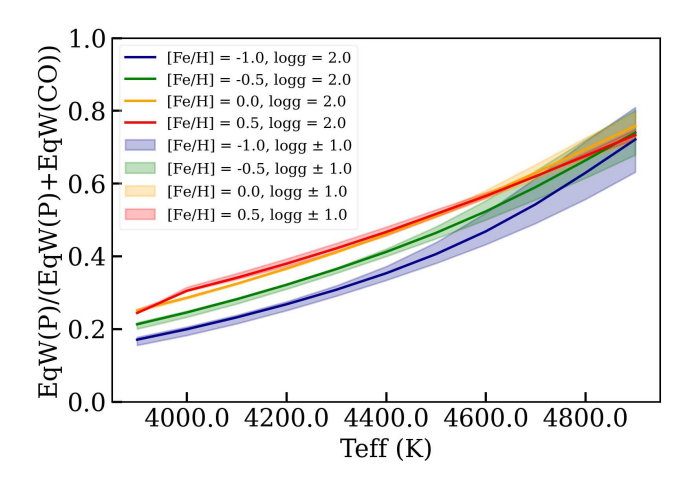


Fig. 9. Fractional contribution of equivalent widths of the P I line in the $CO(\nu=7-4)$ blended line vs. $T_{\rm eff}$ for a set of MARCS (Gustafsson et al. 2008) stellar models in the grid of $3900 \le T_{\rm eff} \le 5000$ K, $1.0 \le \log g \le 3.0$, and [Fe/H]of -1, -0.5, 0.0, and 0.5 dex, all with solar-scaled phosphorus abundances. Different combinations of [Fe/H] and a change in $\log g$ are represented by different colored lines and bands, respectively, with lower $\log g$ at each [Fe/H] resulting in lower equivalent widths for the P I line.

lines and bands, respectively. While the strength of the phosphorus line increases with an increase in $T_{\rm eff}$, the CO line strength becomes weaker at higher $T_{\rm eff}$. As is normal, metal-rich giants have stronger lines, and, for a given metallicity, higher surface gravities, $\log g$, yield weaker lines.

Thus, phosphorus lines are stronger and the $CO(\nu=7-4)$ blend is weaker for giant stars with $T_{\rm eff} > 4500~{\rm K}$ and [Fe/H] >-0.5 dex. For cooler metal-poor stars, the contribution from the phosphorus feature is still significant enough (>15%) to be measurable from a high S/N spectrum, as shown in this work.

Thus we can conclude that the P I line at 16482.92 Å is suitable to estimate phosphorus abundances for K giants at all metallicities. Yet it has to be kept in mind that the contribution from the $CO(\nu = 7-4)$ blend increases with decreasing $T_{\rm eff}$ and [Fe/H]. With the s-rich stars, we have also seen that this line will be useful in the hunt for more P-rich stars.

6. Conclusions

Using high resolution ($R \sim 45\,000$) IGRINS spectra, we determined [P/Fe] for 38 K giant stars in the solar neighborhood based on a detailed spectroscopic analysis of the P I line at 16482.92 Å after a careful handling of the telluric contamination and its elimination, which we show is essential to minimize the uncertainty of the [P/Fe] trend. We show that our [P/Fe] versus [Fe/H] trend within uncertainties is consistent with the results from other studies in the literature. Our trend is higher than the chemical evolution trend from Cescutti et al. (2012) by ~ 0.05 – 0.1 dex, which could mean that the enhancement factor might be higher than 2.75. We also find that the two s-rich stars in our sample exhibit clear enhancements in phosphorus abundance and this warrants a further detailed investigation to understand their possible origins. We further determined abundance ratios of phosphorus with respect to other odd-Z and even-Z elements, estimated from reliable spectral lines in the H- and K-band IGRINS spectra to understand the origin of phosphorus. We find that phosphorus behaves more similarly to α elements than the neighboring odd-Z elements, Na and K, and thus supports the current idea about the contribution of core collapse SNe in the origin and evolution of P. In addition, we find empirical evidence that points to a primary behavior of phosphorus, even though the synthesis of phosphorus occurs due to neutron capture on neutron-rich Si isotopes, which are secondary in nature. Finally we find that although the P I line at 16482.92 Å is suitable to estimate phosphorus abundances for K giants at all metallicities, the weak contribution of the phosphorus feature in cooler metal-poor ($T_{\rm eff} < 4500~{\rm K}, [{\rm Fe/H}] < -0.5$) stars may lead to larger uncertainties in the case of low S/N spectra. We also show that this line will be useful in the hunt for more P-rich stars. Hence, we need more observations with highly capable instruments such as IGRINS that provide a high resolution covering larger spectral orders in order to mitigate the dearth of reliable phosphorus abundance estimates.

Acknowledgements. We thank the anonymous referee for the very constructive comments and suggestions that improved the quality of the paper. G.N. acknowledges the support from the Wenner-Gren Foundations. N.R. acknowledge support from the Royal Physiographic Society in Lund through the Stiftelsen Walter Gyllenbergs fond and Märta och Erik Holmbergs donation. B.T. acknowledges the financial support from the Japan Society for the Promotion of Science as a JSPS International Research Fellow. This work used The Immersion Grating Infrared Spectrometer (IGRINS) was developed under a collaboration between the University of Texas at Austin and the Korea Astronomy and Space Science Institute (KASI) with the financial support of the US National Science Foundation under grants AST-1229522, AST-1702267 and AST-1908892, McDonald Observatory of the University of Texas at Austin, the Korean GMT Project of KASI, the Mt. Cuba Astronomical Foundation and Gemini Observatory. These results made use of the Lowell Discovery Telescope (LDT) at Lowell Observatory. Lowell is a private, non-profit institution dedicated to astrophysical research and public appreciation of astronomy and operates the LDT in partnership with Boston University, the University of Maryland, the University of Toledo, Northern Arizona University and Yale University. This paper includes data taken at The McDonald Observatory of The University of Texas at Austin. The following software and programming languages made this research possible: TOPCAT (version 4.6; Taylor 2005); Python (version 3.8) and its packages ASTROPY (version 5.0; Astropy Collaboration 2022), SCIPY (Virtanen et al. 2020), MATPLOTLIB (Hunter 2007) and NUMPY (van der Walt et al. 2011).

References

```
Afşar, M., Bozkurt, Z., Böcek Topcu, G., et al. 2018a, AJ, 155, 240
Afşar, M., Sneden, C., Wood, M. P., et al. 2018b, ApJ, 865, 44
Arnett, D. 1996, Supernovae and Nucleosynthesis: An Investigation of the His-
   tory of Matter from the Big Bang to the Present (Princeton: Princeton
   University Press)
Asplund, M., Grevesse, N., Sauval, A. J., & Scott, P. 2009, ARA&A, 47, 481
Astropy Collaboration (Price-Whelan, A. M., et al.) 2022, ApJ, 935, 167
Biemont, E., Martin, F., Quinet, P., & Zeippen, C. J. 1994, A&A, 283, 339
Böcek Topcu, G., Afşar, M., Sneden, C., et al. 2019, MNRAS, 485, 4625
Böcek Topcu, G., Afşar, M., Sneden, C., et al. 2020, MNRAS, 491, 544
Brooke, J. S. A., Bernath, P. F., Western, C. M., et al. 2016, J. Quant. Spec.
   Radiat. Transf., 168, 142
Burbidge, E. M., Burbidge, G. R., Fowler, W. A., & Hoyle, F. 1957, Rev. Mod.
  Phys., 29, 547
Caffau, E., Bonifacio, P., Faraggiana, R., & Steffen, M. 2011, A&A, 532, A98
Caffau, E., Andrievsky, S., Korotin, S., et al. 2016, A&A, 585, A16
Caffau, E., Bonifacio, P., Oliva, E., et al. 2019, A&A, 622, A68
Cescutti, G., Matteucci, F., Caffau, E., & François, P. 2012, A&A, 540, A33
Chieffi, A., & Limongi, M. 2004, ApJ, 608, 405
Clayton, D. 2003, Handbook of Isotopes in the Cosmos (Cambridge, UK:
   Cambridge University Press)
Fanelli, C., Origlia, L., Oliva, E., et al. 2021, A&A, 645, A19
```

Forsberg, R., Jönsson, H., Ryde, N., & Matteucci, F. 2019, A&A, 631, A113

Grevesse, N., Asplund, M., & Sauval, A. J. 2007, Space Sci. Rev., 130, 105

Gustafsson, B., Edvardsson, B., Eriksson, K., et al. 2008, A&A, 486, 951

Han, J.-Y., Yuk, I.-S., Ko, K., et al. 2012, SPIE Conf. Ser., 8550, 85501B

Hawkins, K., Masseron, T., Jofré, P., et al. 2016, A&A, 594, A43
Hayes, C. R., Masseron, T., Sobeck, J., et al. 2022, ApJS, 262, 34
Hinkle, K. H., Wallace, L., & Livingston, W. 1995, PASP, 107, 1042

Forsberg, R., Ryde, N., Jönsson, H., Rich, R. M., & Johansen, A. 2022, A&A,

Gully-Santiago, M., Wang, W., Deen, C., & Jaffe, D. 2012, SPIE Conf. Ser.,

```
Jönsson, H., Allende Prieto, C., Holtzman, J. A., et al. 2018, AJ, 156, 126
Karakas, A. I. 2010, MNRAS, 403, 1413
Kausch, W., Noll, S., Smette, A., et al. 2015, A&A, 576, A78
Kimble, R. A., Woodgate, B. E., Bowers, C. W., et al. 1998, ApJ, 492, L83
Kobayashi, C., Umeda, H., Nomoto, K., Tominaga, N., & Ohkubo, T. 2006, ApJ,
   653, 1145
Lee, J.-J., Gullikson, K., & Kaplan, K. 2017, https://doi.org/
   10.5281/zenodo.845059
Li, G., Gordon, I. E., Rothman, L. S., et al. 2015, ApJS, 216, 15
Lomaeva, M., Jönsson, H., Ryde, N., Schultheis, M., & Thorsbro, B. 2019, A&A,
   625, A141
Maas, Z. G., Pilachowski, C. A., & Cescutti, G. 2017, ApJ, 841, 108
Maas, Z. G., Cescutti, G., & Pilachowski, C. A. 2019, AJ, 158, 219
Maas, Z. G., Hawkins, K., Hinkel, N. R., et al. 2022, AJ, 164, 61
Mace, G., Kim, H., Jaffe, D. T., et al. 2016, SPIE Conf. Ser., 9908, 99080C
Mace, G., Sokal, K., Lee, J.-J., et al. 2018, SPIE Conf. Ser., 10702, 107020Q
Mahadevan, S., Ramsey, L., Bender, C., et al. 2012, SPIE Conf. Ser., 8446,
   84461S
Mahadevan, S., Ramsey, L. W., Terrien, R., et al. 2014, SPIE Conf. Ser., 9147,
   91471G
Majewski, S. R., Schiavon, R. P., Frinchaboy, P. M., et al. 2017, AJ, 154, 94
Masseron, T., Merle, T., & Hawkins, K. 2016, Astrophysics Source Code Library
   [record ascl:1605.004]
Masseron, T., García-Hernández, D. A., Santoveña, R., et al. 2020a, Nat.
   Commun., 11, 375
Masseron, T., García-Hernández, D. A., Zamora, O., & Manchado, A. 2020b,
   ApJ, 904, L1
Matteucci, F. 2021, A&AR, 29, 5
Montelius, M., Forsberg, R., Ryde, N., et al. 2022, A&A, 665, A135
Moon, B., Wang, W., Park, C., et al. 2012, SPIE Conf. Ser., 8450, 845048
Nomoto, K., Kobayashi, C., & Tominaga, N. 2013, ARA&A, 51, 457
Oh, J. S., Park, C., Cha, S.-M., et al. 2014, SPIE Conf. Ser., 9147, 914739
Origlia, L., Oliva, E., Baffa, C., et al. 2014, SPIE Conf. Ser., 9147, 91471E
Park, C., Jaffe, D. T., Yuk, I.-S., et al. 2014, SPIE Conf. Ser., 9147, 91471D
Pendlebury, J. M., & Smith, K. F. 1964, Proc. Phys. Soc., 84, 849
Prantzos, N., Abia, C., Limongi, M., Chieffi, A., & Cristallo, S. 2018, MNRAS,
   476, 3432
Roederer, I. U., Jacobson, H. R., Thanathibodee, T., Frebel, A., & Toller, E. 2014,
   ApJ, 797, 69
Ryde, N., Jönsson, H., Mace, G., et al. 2020, ApJ, 893, 37
Santos-Peral, P., Recio-Blanco, A., de Laverny, P., Fernández-Alvar, E., &
   Ordenovic, C. 2020, A&A, 639, A140
Shetrone, M., Bizyaev, D., Lawler, J. E., et al. 2015, ApJS, 221, 24
Smette, A., Kausch, W., Sana, H., et al. 2015, Astrophysics Source Code Library
   [record ascl:1501.013]
Sneden, C., Lucatello, S., Ram, R. S., Brooke, J. S. A., & Bernath, P. 2014, ApJS,
   214, 26
Sneden, C., Afşar, M., Bozkurt, Z., et al. 2021, AJ, 161, 128
Struve, O. 1930, ApJ, 71, 150
Taylor, M. B. 2005, ASP Conf. Ser., 347, 29
Telting, J. H., Avila, G., Buchhave, L., et al. 2014, Astron. Nachr., 335, 41
Tody, D. 1993, ASP Conf. Ser., 52, 173
Valenti, J. A., & Piskunov, N. 1996, A&As, 118, 595
Valenti, J. A., & Piskunov, N. 2012, Astrophysics Source Code Library [record
   ascl:1202.013]
van der Walt, S., Colbert, S. C., & Varoquaux, G. 2011, Comput. Sci. Eng., 13,
Virtanen, P., Gommers, R., Oliphant, T. E., et al. 2020, Nat. Methods, 17, 261
Wallace, L., & Livingston, W. 2003, An atlas of the solar spectrum in the
   infrared from 1850 to 9000 cm-1 (1.1 to 5.4 micrometer), (Tucson: National
   Solar Observatory, National Optical Astronomy Observatory, NSO Technical
   Report)
Wang, W., Gully-Santiago, M., Deen, C., Mar, D. J., & Jaffe, D. T. 2010, SPIE
   Conf. Ser., 7739, 77394L
Weinberg, D. H., Holtzman, J. A., Hasselquist, S., et al. 2019, ApJ, 874, 102
Weinberg, D. H., Holtzman, J. A., Johnson, J. A., et al. 2022, ApJS, 260, 32
Woodgate, B. E., Kimble, R. A., Bowers, C. W., et al. 1998, PASP, 110, 1183 Woosley, S. E., & Weaver, T. A. 1995, ApJS, 101, 181
```

Yuk, I.-S., Jaffe, D. T., Barnes, S., et al. 2010, SPIE Conf. Ser., 7735, 77351M

Hinkle, K. H., Cuberly, R. W., Gaughan, N. A., et al. 1998, SPIE Conf. Ser.,

Hinkel, N. R., Hartnett, H. E., & Young, P. A. 2020, ApJ, 900, L38

Hunter, J. D. 2007, Comput. Sci. Eng., 9, 90

Holtzman, J. A., Shetrone, M., Johnson, J. A., et al. 2015, AJ, 150, 148

Jeong, U., Chun, M.-Y., Oh, J. S., et al. 2014, SPIE Conf. Ser., 9154, 91541X

Iwamoto, K., Brachwitz, F., Nomoto, K., et al. 1999, ApJS, 125, 439Jacobson, H. R., Thanathibodee, T., Frebel, A., et al. 2014, ApJ, 796, L24

Jönsson, H., Ryde, N., Nordlander, T., et al. 2017, A&A, 598, A100

666, A125

8450, 84502S

Appendix A: Tables

Table A.1. Wavelengths of the lines for the elements Mg, Al, Si, S, and K in IGRINS H and K bands used to determine their respective abundances for the stars in our sample.

Element	Wavelength (Å)
	16373.87
	16388.85
	17227.70
Na	22056.43
	22083.66
	23348.42
	23379.14
	15740.70
Mg	15748.89
	17108.63
	16718.97
A1	16750.60
Ai	16763.37
	17699.05
	15361.16
	16163.71
Si	16343.93
	16828.18
	17225.63
	15469.82
	15478.48
	22006.41
_	22507.60
S	22519.11
	22526.05
	22552.61
	22563.87
	22575.43
K	15163.09
	15168.40

Table A.2. [C/Fe], [N/Fe], and [O/Fe] abundances and their uncertainties determined in this work.

Star	[C/Fe]	σ [C/Fe]	[N/Fe]	σ[N/Fe]	[O/Fe]	σ [O/Fe]	
		dex	dex	dex	dex	dex	
$\alpha \mathrm{Boo}^*$	0.19	0.07	0.3	0.06	0.51	0.06	
μ Leo	0.06	0.05	0.49	0.05	0.1	0.05	
ϵVir	-0.18	0.09	0.71	0.04	0.31	0.04	
betaGem	-0.08	0.08	0.38	0.05	0.07	0.05	
HD 102328	0.12	0.06	0.39	0.03	0.11	0.03	
HIP50583	-0.03	0.06	0.39	0.03	0.19	0.03	
HIP63432	0.15	0.07	0.48	0.06	0.46	0.06	
HIP72012	-0.03	0.08	0.3	0.07	0.17	0.07	
HIP90344	0.12	0.08	0.25	0.05	0.31	0.05	
HIP96014	0.12	0.06	0.22	0.03	0.19	0.03	
HIP102488	0.0	0.07	0.33	0.05	0.24	0.05	
2M16113361	0.09	0.08	0.16	0.08	0.48	0.08	
2M17215666	0.11	0.07	0.39	0.05	0.6	0.05	
KIC3748585	-0.0	0.05	0.39	0.05	0.11	0.05	
KIC3955590	0.05	0.03	0.36	0.05	0.09	0.05	
KIC3936921	0.08	0.07	0.27	0.03	0.15	0.03	
KIC4659706	0.14	0.07	0.34	0.12	0.17	0.12	
KIC5113061	0.0	0.06	0.34	0.05	0.08	0.05	
KIC5113910	0.01	0.06	0.4	0.05	0.19	0.05	
KIC5709564	0.16	0.06	0.28	0.11	0.41	0.11	
KIC5779724	0.17	0.03	0.28	0.07	0.43	0.07	
KIC5859492	0.02	0.05	0.38	0.03	0.06	0.03	
KIC5900096	0.1	0.07	0.36	0.05	0.1	0.05	
KIC6465075	0.12	0.15	0.21	0.05	0.19	0.05	
KIC6837256	0.21	0.05	0.3	0.04	0.48	0.04	
KIC7006979	0.03	0.06	0.43	0.05	0.4	0.05	
KIC10186608	0.11	0.05	0.21	0.03	0.16	0.03	
KIC11045542	0.1	0.05	0.3	0.04	0.24	0.04	
KIC11342694	0.07	0.05	0.16	0.03	0.07	0.03	
KIC11444313	0.02	0.06	0.32	0.03	0.1	0.03	
KIC11569659	0.16	0.08	0.26	0.16	0.29	0.16	
ξHya	-0.49	0.05	0.78	0.04	0.1	0.04	
HD175541	-0.08	0.04	0.38	0.08	0.24	0.08	
HD176981	-0.05	0.05	0.27	0.08	0.07	0.08	
HD206610	0.1	0.03	0.38	0.06	0.19	0.06	
HD76445	0.08	0.09	0.37	0.03	0.32	0.03	
NGC67051184	0.02	0.07	0.32	0.04	0.03	0.04	
NGC67051423	0.01	0.07	0.35	0.04	0.01	0.04	

Table A.3. Mean abundances of Na, Mg, Al, Si, S, and K and their uncertainties based on a line-by-line analysis using the lines listed in Table A.1

			$[X/Fe] \pm \sigma[X/Fe]$			
Star	Na	Mg	Al	Si	S	K
α Boo	0.1 ± 0.08	0.49 ± 0.04	0.29 ± 0.07	0.3 ± 0.07	0.37 ± 0.19	0.27 ± 0.02
μ Leo	0.24 ± 0.11	0.16 ± 0.03	0.1 ± 0.05	0.0 ± 0.09	0.1 ± 0.11	0.08 ± 0.08
ÉpsVir	0.19 ± 0.06	-0.05 ± 0.01	0.0 ± 0.03	0.03 ± 0.01	0.06 ± 0.07	0.04 ± 0.02
β Gem	0.09 ± 0.06	-0.01 ± 0.01	-0.03 ± 0.05	-0.01 ± 0.04	0.0 ± 0.11	0.04 ± 0.05
HD 102328	0.16 ± 0.08	0.07 ± 0.02	0.06 ± 0.04	0.0 ± 0.07	0.04 ± 0.07	0.04 ± 0.09
HIP50583	0.02 ± 0.08	0.11 ± 0.08	0.14 ± 0.08	0.28 ± 0.05	0.19 ± 0.19	0.01 ± 0.11
HIP63432	0.02 ± 0.04	0.42 ± 0.05	0.2 ± 0.12	0.38 ± 0.04	0.45 ± 0.24	0.17 ± 0.03
HIP72012	-0.01 ± 0.04	0.23 ± 0.04	0.06 ± 0.05	0.03 ± 0.06	0.24 ± 0.16	-0.0 ± 0.0
HIP90344	0.04 ± 0.05	0.15 ± 0.02	0.13 ± 0.08	0.11 ± 0.06	0.12 ± 0.1	0.08 ± 0.08
HIP96014	0.05 ± 0.05	0.24 ± 0.02	0.17 ± 0.04	0.2 ± 0.03	0.14 ± 0.12	0.09 ± 0.03
HIP102488	0.04 ± 0.05	0.15 ± 0.01	0.14 ± 0.04	0.11 ± 0.01	0.07 ± 0.07	0.16 ± 0.03
2M16113361	0.13 ± 0.23	0.46 ± 0.04	0.08 ± 0.14	0.25 ± 0.17	0.23 ± 0.4	0.0 ± 0.0
2M17215666	0.07 ± 0.19	0.57 ± 0.05	0.36 ± 0.21	0.6 ± 0.03	0.39 ± 0.31	0.0 ± 0.0
KIC3748585	0.1 ± 0.08	0.06 ± 0.02	0.06 ± 0.03	0.03 ± 0.04	0.12 ± 0.1	0.16 ± 0.04
KIC3936921	0.0 ± 0.07	0.26 ± 0.03	0.06 ± 0.02	0.11 ± 0.03	0.18 ± 0.12	0.03 ± 0.1
KIC3955590	0.14 ± 0.08	0.14 ± 0.01	0.1 ± 0.05	0.09 ± 0.06	0.21 ± 0.15	0.07 ± 0.04
KIC4659706	0.06 ± 0.08	0.14 ± 0.01	0.07 ± 0.07	0.04 ± 0.04	0.08 ± 0.1	0.02 ± 0.05
KIC5113061	0.16 ± 0.07	0.19 ± 0.04	0.01 ± 0.04	0.12 ± 0.05	0.24 ± 0.19	0.04 ± 0.04
KIC5113910	0.17 ± 0.04	0.3 ± 0.03	0.2 ± 0.05	0.25 ± 0.04	0.26 ± 0.17	0.1 ± 0.1
KIC5709564	0.12 ± 0.09	0.42 ± 0.02	0.28 ± 0.04	0.3 ± 0.04	0.25 ± 0.16	0.25 ± 0.0
KIC5779724	0.12 ± 0.09	0.44 ± 0.02	0.28 ± 0.06	0.27 ± 0.04	0.31 ± 0.19	0.27 ± 0.04
KIC5859492	0.06 ± 0.04	0.15 ± 0.01	0.06 ± 0.06	0.09 ± 0.03	0.12 ± 0.11	0.02 ± 0.02
KIC5900096	0.1 ± 0.08	0.04 ± 0.09	0.07 ± 0.05	0.02 ± 0.04	0.06 ± 0.08	0.01 ± 0.03
KIC6465075	0.07 ± 0.07	0.23 ± 0.02	0.17 ± 0.03	0.19 ± 0.03	0.11 ± 0.15	0.09 ± 0.09
KIC6837256	0.16 ± 0.11	0.48 ± 0.02	0.38 ± 0.02	0.33 ± 0.05	0.3 ± 0.16	0.37 ± 0.03
KIC7006979	0.13 ± 0.14	0.16 ± 0.03	0.12 ± 0.07	0.1 ± 0.03	0.18 ± 0.26	0.04 ± 0.04
KIC10186608	0.01 ± 0.07	0.06 ± 0.07	0.08 ± 0.03	0.16 ± 0.06	0.07 ± 0.11	0.06 ± 0.07
KIC11045542	0.09 ± 0.13	0.2 ± 0.14	0.18 ± 0.11	0.19 ± 0.09	0.18 ± 0.21	0.04 ± 0.04
KIC11342694	0.04 ± 0.12	0.14 ± 0.01	0.1 ± 0.03	0.05 ± 0.04	0.06 ± 0.14	0.06 ± 0.06
KIC11444313	0.09 ± 0.05	0.21 ± 0.04	0.16 ± 0.05	0.15 ± 0.05	0.21 ± 0.14	0.1 ± 0.01
KIC11569659	0.11 ± 0.1	0.28 ± 0.01	0.2 ± 0.05	0.21 ± 0.05	0.23 ± 0.2	0.17 ± 0.06
<i>ξ</i> Hya	0.05 ± 0.08	-0.02 ± 0.02	-0.02 ± 0.05	-0.08 ± 0.1	-0.07 ± 0.14	-0.01 ± 0.02
HD175541	0.0 ± 0.0	0.03 ± 0.0	0.04 ± 0.04	0.07 ± 0.04	0.02 ± 0.02	0.08 ± 0.01
HD176981	0.07 ± 0.09	0.12 ± 0.1	0.06 ± 0.04	0.08 ± 0.08	0.18 ± 0.03	0.02 ± 0.0
HD206610	0.06 ± 0.05	0.09 ± 0.0	0.11 ± 0.03	0.07 ± 0.01	0.07 ± 0.01	0.07 ± 0.01
HD76445	0.04 ± 0.05	0.3 ± 0.05	0.27 ± 0.02	0.16 ± 0.09	0.23 ± 0.01	0.25 ± 0.02
NGC67051184	0.15 ± 0.09	0.2 ± 0.03	0.12 ± 0.07	0.16 ± 0.05	0.32 ± 0.0	0.05 ± 0.02
NGC67051423	0.26 ± 0.09	0.13 ± 0.09	0.1 ± 0.04	0.1 ± 0.06	0.33 ± 0.04	-0.05 ± 0.01